01 Jan 2008

A Comparison of Alternating Minimization and Expectation Maximization Algorithms for Single Source Gamma Ray Tomography

R. Varma

S. Bhusarapu

J. A. O'Sullivan

M. (Muthanna) H. Al-Dahhan
Missouri University of Science and Technology, aldahhanm@mst.edu

Recommended Citation

R. Varma et al., "A Comparison of Alternating Minimization and Expectation Maximization Algorithms for Single Source Gamma Ray Tomography," *Measurement Science and Technology*, vol. 19, no. 1, article no. 015506, IOP Publishing, Jan 2008.
The definitive version is available at https://doi.org/10.1088/0957-0233/19/1/015506

A comparison of alternating minimization and expectation maximization algorithms for single source gamma ray tomography

Meas. Sci. Technol. **19** (2008) 015506 (13pp) doi:10.1088/0957-0233/19/1/015506

A comparison of alternating minimization and expectation maximization algorithms for single source gamma ray tomography

R Varma[1], S Bhusarapu[2], J A O'Sullivan[3] and M H Al-Dahhan[1,4]

[1] Chemical Reaction Engineering Laboratory, Department of Energy, Environment and Chemical Engineering, Campus Box 1198, 1 Brookings Drive, Washington University, St Louis, MO 63130, USA
[2] Harper International Corporation, West Drullard Avenue, Lancaster, NY 14086, USA
[3] Electronic Systems and Signals Research Laboratory, Department of Electrical and Systems Engineering, 1 Brookings Drive, Washington University, St Louis, MO 63130-4899, USA

E-mail: varma@wustl.edu, sbhusarapu@harperintl.com, jao@wustl.edu and muthanna@che.wustl.edu

Received 5 March 2007, in final form 28 September 2007
Published 30 November 2007
Online at stacks.iop.org/MST/19/015506

Abstract
Lange and Carson (1984 *J. Comput. Assist. Tomogr.* **8** 306–16) defined image reconstruction for transmission tomography as a maximum likelihood estimation problem and derived an expectation maximization (EM) algorithm to obtain the maximum likelihood image estimate. However, in the maximization step or M-step of the EM algorithm, an approximation is made in the solution which can affect the image quality, particularly in the case of domains with high attenuating material. O'Sullivan and Benac (2007 *IEEE Trans. Med. Imaging* **26** 283–97) reformulated the maximum likelihood problem as a double minimization of an I-divergence to obtain a family of image reconstruction algorithms, called the alternating minimization (AM) algorithm. The AM algorithm increases the log-likelihood function while minimizing the I-divergence. In this work, we implement the AM algorithm for image reconstruction in gamma ray tomography for industrial applications. Experimental gamma ray transmission data obtained with a fan beam geometry gamma ray scanner, and simulated transmission data based on a synthetic phantom, with two phases (water and air) were considered in this study. Image reconstruction was carried out with these data using the AM and the EM algorithms to determine and quantitatively compare the holdup distribution images of the two phases in the phantoms. When compared to the EM algorithm, the AM algorithm shows qualitative and quantitative improvement in the holdup distribution images of the two phases for both the experimental and the simulated gamma ray transmission data.

Keywords: alternating minimization, expectation maximization, computed tomography, I-divergence, image reconstruction, log likelihood, multiphase systems, two phase flow

(Some figures in this article are in colour only in the electronic version)

Notation used

$d(y)$	Photon counts received by detector y
$E[\bullet]$	Mean of the given function
$g(y:\mu)$	Mean value of photon counts received for a given y and μ
$h(y\|x)$	Length of the segment of projection y in pixel x (cm)
I	Number of photon counts generated by simulation
$I(a\|\|b)$	I-divergence of quantities a and b
$M(y\|x)$	Conditioned expected values of photons that enter pixel x along projection y
n	Number of samples of count data used to estimate the mean counts for each projection

[4] Corresponding author.

$N(y\|x)$	Conditioned expected values of photons that survive and leave pixel x along projection y
$p_{X(y\|x)}$	Probability of a complete data set
x	Index for pixel in image space
$X(y\|x)$	Random number of photons entering a pixel x along projection y
y	Index for projection or source detector pair

Greek

$\varepsilon(x)$	Holdup fraction of any given phase
λ	Source intensity (counts)
$\hat{\mu}(x)$	Attenuation values estimated by algorithm for a given pixel x (cm^{-1})
$\mu_{\text{Phantom}}(x)$	Attenuation value of a simulated phantom for which transmission data are generated (cm^{-1})

Subscripts

l	System filled with liquid
g	System filled with gas
$l-g$	System filled with liquid and gas
$l-g-s$	System filled with liquid, gas and solid

1. Introduction

Computed tomography has been successfully used in the medical field for radiology diagnostics. Recently, its use has been expanded to process engineering for industrial applications, in particular for visualizing the flow field in multiphase flow systems (Kumar and Duduković 1997). One key area of research addresses the improvement of image reconstruction algorithms. Several authors have made contributions to the theory of reconstructive tomography, and an early overview of such algorithms was presented by Snyder and Cox (1977).

Algebraic algorithms such as Fourier/convolution techniques when applied to determine the phase holdup distribution in two phase systems either assume the systems to be azimuthally symmetric in distribution or consider the gamma ray transmission process to be deterministic thereby completely ignoring the stochastic nature of the data (Bieberle and Hampel 2006). Expectation maximization (EM) (Lange and Carson 1984) and alternating minimization (AM) (O'Sullivan and Benac 2007) algorithms account for the stochastic nature of the gamma ray transmission across the domain of interest. This makes these algorithms more favorable for image reconstruction to determine the phase holdup distribution.

The EM algorithm has been extensively used to process gamma ray tomography data to image holdup distribution in various two phase systems. Some of its applications include imaging, gas holdup in a gas liquid bubble column (Kumar *et al* 1997), solids holdup in a liquid–solid riser (Roy *et al* 1997), liquid flow distribution in structured packing (Roy *et al* 2004) and monolith reactor (Roy and Al-Dahhan 2005), and gas holdup in stirred tanks (Khopkar *et al* 2005). This study applies the AM algorithm proposed for transmission tomography by O'Sullivan and Benac (2007) for the case of single energy gamma ray tomography for imaging phase holdup distribution in two phase systems. Phantoms used for this study are designed to represent multiphase systems studied with EM. Both the AM and EM algorithms are applied to the phantoms. The holdup distribution results obtained with the AM algorithm are quantitatively compared with those obtained with the EM algorithm as proposed by Lange and Carson (1984), for simulated and experimental gamma ray transmission data from phantoms containing two phases. In addition, the holdup distribution images using the filter back projection (FBP) method as proposed by Kak and Slaney (1988) have been included for qualitative comparison with the images obtained with the AM and EM algorithms. The FBP is a noniterative technique and does not account for the stochastic nature of gamma ray photon emission.

2. The algorithms

Since the objective of this study is to primarily compare the AM and the EM algorithms, these algorithms have been briefly discussed and outlined for the purpose of continuity and for the benefit of the uninitiated reader. Since the FBP method is well established, it has not been discussed here. For further information, the reader is encouraged to read the relevant references cited.

2.1. Expectation maximization algorithm

Lange and Carson (1984) defined the image reconstruction for tomography as a maximum likelihood estimation problem and derived an EM algorithm to obtain the maximum likelihood image estimate. In experiments where gamma ray counts statistics is high (∼500 counts/projection), ignoring the true statistical nature of the data may not be a serious limitation because Poisson counting noise is only a component of the total system noise (Lange and Carson 1984). It is precisely in the low count experiments (<100 counts/projection) that the EM algorithm is expected to provide the greatest improvement in the reconstruction quality. Usually in transmission tomography experiments with the amount of shielding provided at the detectors' end (to increase the spatial resolution), the counts recorded are bound to be small (∼100 or less counts/projection), which forces one to use an EM algorithm. Superiority of the EM algorithms over Fourier techniques and non-iterative algebraic methods such as the incorporation of non-negativity constraints and objective measure of quality of reconstruction (e.g. log-likelihood, least squares, maximum entropy) is discussed in detail by Lange and Carson (1984).

The EM algorithm is a general iterative technique for computing maximum likelihood estimates in any general scenario of measurement of statistical quantities. Application to image reconstruction in transmission tomography is only a specific application. Each iteration of the EM algorithm consists of two steps: expectation (E step) and maximization (M step). The derivation of the E and M steps for transmission

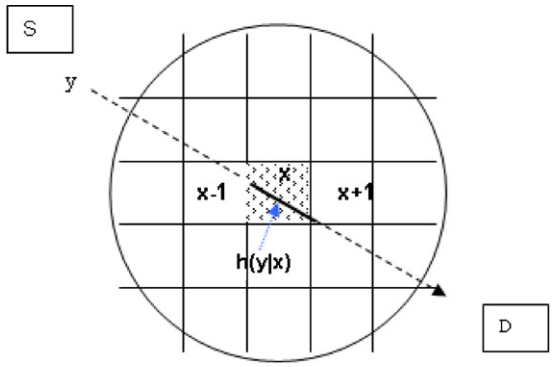

Figure 1. Schematic of the representation of a transmission tomography domain; the boxes represent the pixels. Here S: source, D: detector, y: projection index, x: pixel index and $h(y|x)$ is the segment of projection y in pixel x.

tomography is discussed in detail by Lange and Carson (1984). Some of the key elements are highlighted here.

In the E-step, the conditional expectation of 'entire' or 'complete' data set is estimated on the basis of the measured data (counts from the detector) and the parameter set (attenuation values). The 'complete' data set represents intensity of the photons that enter and leave each pixel in the domain for all the projections. If for a given pixel x along a projection y (figure 1), we define $X(y|x)$ as the random number of photons (or counts) that enter x and $X(y|(x+1))$ the random number that survive and leave x, then this process can be modeled as a binomial distribution with two outcomes: survival of the photons $\exp(-h(y|x)\mu(x))$ and absorption of the photons $[1-\exp(-h(y|x)\mu(x))]$, where $h(y|x)$ is the segment of projection y in pixel x. The probability of this binomial process can be represented by (1); in other words, (1) represents the probability of the 'complete' data set for pixel x:

$$p_{X(y|(x+1))} = \begin{pmatrix} X(y|x) \\ X(y|(x+1)) \end{pmatrix} [\exp(-h(y|x)\mu(x))]^{X(y|(x+1))} \times [1-\exp(-h(y|x)\mu(x))]^{X(y|x)-X(y|(x+1))}. \quad (1)$$

The first pixel along any projection y receives the photons emitted from the gamma source. This is a Poisson process with mean λ which represents the intensity of the source; its probability is given by

$$p_{(X(y|1))} = \frac{\lambda^{X(y|1)}\exp(-\lambda)}{X(y|1)!}. \quad (2)$$

Since the pixels are independent, the likelihood function of the entire 'complete' data set (for all pixels along projection y) can be represented as the product of the individual likelihood functions of each pixel that lies along a projection y. This likelihood function is represented as

$$f(N(y):\mu) = \frac{\lambda^{X(y|1)}\exp(-\lambda)}{X(y|1)!} \prod_{x\in X} \begin{pmatrix} X(y|x) \\ X(y|(x+1)) \end{pmatrix} \times [\exp(-h(y|x)\mu(x)]^{X(y|(x+1))} \times [1-\exp(-h(y|x)\mu(x)]^{(X(y|x)-X(y|(x+1)))}. \quad (3)$$

If the complete data set was known, then computing the attenuation values $\mu(x)$ for every pixel would be straightforward. However, this is not the case since only the count data observed by the detectors representing the random number of photons that have survived all the pixels along a projection are available. The expectation step involves computing the expectation of the 'complete' data set for a given pixel, conditional to the observed data $d(y)$ (measured by detector D) given the current estimate of the attenuation function $\hat{\mu}^{(k)}(x)$ as given by

$$E[X(y|x)|d(y), \hat{\mu}^{(k)}(x)]. \quad (4)$$

Lange and Carson (1984) show that (4) can be represented as

$$E[X(y|x)|d(y)] = d(y) + E[X(y|x)] - E[d(y)]. \quad (5)$$

Equation (5) is used to compute $M(y|x)$ and $N(y|x)$, the expected values of the photons entering and leaving given pixel x respectively along projection y. The entities $M(y|x)$ and $N(y|x)$ are the conditional expectations related to $X(y|x)$ and $X(y|(x+1))$, respectively, by (4).

In the M-step, this conditional expectation is maximized with respect to a parameter set. In the case of gamma ray transmission tomography, the parameter set is the attenuation values $\mu(x)$ of the pixels in the scanned domain and the measured data set $d(y)$ is the detector signal obtained for each projection y. Equation (5) is used to determine the conditional expectation values $M(y|x)$ and $N(y|x)$ for each pixel in the image which is then summed over all projections and then substituted in the likelihood function. The natural logarithm of this equation is given by (6), which represents the log likelihood of the 'complete' data set over all projections y:

$$\ln[f(N(y):\mu)] = \sum_{y\in Y}\sum_{x\in X}\{N(y|x) \times \ln[\exp(-h(y|x)\mu(x))] + (M(y|x) - N(y|x)) \times \ln[1-\exp(-h(y|x)\mu(x))]\} + R, \quad (6)$$

where R represents all the terms that are not dependent on $\mu(x)$. Maximizing (6) by setting the value of the partial derivative with respect to $\mu(x)$ to zero yields a transcendental equation

$$\sum_{y\in Y} -N(y|x)h(y|x) + \sum_{y\in Y}[M(y|x) - N(y|x)] \times \frac{h(y|x)}{\exp[h(y|x)\mu(x)] - 1} = 0. \quad (7)$$

Since (7) cannot be solved exactly due to the exponential term, Lange and Carson (1984) suggest the Taylor-series-based approximation to simplify the solution:

$$\frac{1}{\exp[h(y|x)\mu(x)] - 1} = \frac{1}{h(y|x)\mu(x)} - \frac{1}{2} + \frac{h(y|x)\mu(x)}{12} + O\{[h(y|x)\mu(x)]^3\}. \quad (8)$$

The authors recommend using the first three terms of (8) to arrive at (9) in order to make a good approximation of (7):

$$0 = \mu(x)^2 \cdot \sum_{y\in Y} [M(y|x) - N(y|x)] \frac{h(y|x)^2}{12} - \mu(x) \cdot \sum_{y\in Y} [M(y|x) + N(y|x)] \frac{h(y|x)}{2} + \sum_{y\in Y} [M(y|x) - N(y|x)]. \quad (9)$$

Equation (9) is a quadratic equation which has a solution given by

$$\hat{\mu}(x)^{(k+1)} = B/2A - \sqrt{B^2 - 4AC}/2A, \quad (10a)$$

where

$$A = \sum_{y\in Y} [M(y|x) - N(y|x)] \frac{h(y|x)^2}{12},$$
$$B = \sum_{y\in Y} [M(y|x) - N(y|x)] \frac{h(y|x)}{2} \quad (10b)$$
$$C = \sum_{y\in Y} [M(y|x) - N(y|x)].$$

The iterative process starts with an initial guess for $\hat{\mu}(x)^k$ ($k = 0$); this is used to compute the conditional expectation values of $M(y|x)$ and $N(y|x)$ using $d(y)$ based on (5). These values are then used to determine the next estimate of attenuation $\hat{\mu}(x)^{k+1}$ based on (10). By setting $k = k + 1$, this process is repeated starting from (5) till the value of $\hat{\mu}(x)^{k+1}$, which maximizes the log likelihood of the complete data set, is reached.

The approximation for (7) given by (8), as discussed in the previous paragraph, is valid for small values of $(h(y|x)\mu(x))$ and is not accurate for applications involving regions of high density, high mass attenuation $\mu(x)/\rho$ (cm^2 g^{-1}), or for coarse pixel resolution, where the values of $h(y|x)$ are large. This in turn may lead to a decrease in the log-likelihood function from one iteration to the other instead of an increase. This is a major shortcoming for imaging applications involving industrial multiphase flow systems as they are usually constructed with metals or have internal structures that are also made of metal. To improve accuracy, other authors have used modified approaches to derive the M-step (Ollinger 1994) or the E-step (Browne and Holmes 1992) of the EM algorithm in the context of its application to positron emission tomography (PET). Although these approaches can be adapted to image reconstruction in gamma ray transmission tomography for further improvement, the work by Lange and Carson (1984) has been compared here to the AM algorithm as there is precedence for its use in determining phase holdup distribution in multiphase systems using gamma ray tomography.

2.2. Alternating minimization algorithm

The expectation maximization algorithm is a special case of the alternating minimization (O'Sullivan and Benac 2007) algorithm, which has been extensively studied in the applications involving x-ray-based medical imaging (Benac 2005). The AM algorithm could potentially be used for other applications which involve either gamma ray or x-ray transmission tomography. O'Sullivan and Benac (2007) reformulated the maximum likelihood problem as a double minimization of an I-divergence to obtain a family of image reconstruction algorithms. I-divergence, introduced by Csiszár (1991), is a measure of discrepancy between two functions $a(y)$ and $b(y)$, which is given as

$$I(a\|b) = \sum_{y\in Y} \left\{ a(y) \ln \left[\frac{a(y)}{b(y)} \right] - [a(y) - b(y)] \right\}, \quad (11)$$

where y is a finite dimensional space.

Csiszár (1991) examined a wide variety of discrepancy measures (e.g. least squares, entropy) including the I-divergence measure (11) between two functions $a(y)$ and $b(y)$ and arrived at the following conclusion which is relevant for the image reconstruction problem subject to non-negativity constraints. Csiszár (1991) concluded that if the functions involved are all real valued, having both positive and negative values, then minimizing the least squares is the only consistent choice, whereas if all the functions are required to be non-negative, then minimizing the I-divergence is the only consistent choice. This I-divergence measure was first employed for image reconstruction by Snyder *et al* (1992).

Each step of minimization in the AM algorithm is claimed to be an exact process, without any approximation as in the case of EM (8), which represents one of its advantages over the EM algorithm. The alternating minimization algorithm formulated by O'Sullivan and Benac (2007) is guaranteed to monotonically increase the log-likelihood function at every iteration. In this work, the AM algorithm is applied for the first time to the image phase holdup distribution using gamma ray tomography to seek improvements in the quality of holdup distribution images for industrial multiphase flow systems.

The image reconstruction algorithm is based on a statistical model for the measured data, Beer's law and a realistic model for the known point spread function (O'Sullivan and Benac 2007). The reconstruction problem is formulated as an optimization (maximum likelihood) problem in the statistical estimation theory.

A brief outline of the algorithm is described below. For more details, the reader is encouraged to refer to O'Sullivan and Benac (2007). If we define $g(y : \mu)$ as the mean of the counts $d(y)$ received by the detector (a Poisson random number) per Beer–Lambert's law, then

$$g(y : \mu) = \lambda(y) \exp \left[- \sum_{x\in X} h(y|x)\mu(x) \right]. \quad (12)$$

In the expression for the I-divergence, the function $a(y)$ is taken to be the measured data represented by $d(y)$ and $b(y)$ is taken to be a nonlinear model $q(y)$ representing the transmission of the photons. The term $q(y)$ includes the parameter set $\hat{\mu}(x)$, which is to be estimated:

$$q(y) = \lambda(y) \exp \left[- \sum_{x\in X} h(y|x)\hat{\mu}(x) \right]. \quad (13)$$

If (11) is written for this case as

$$I(d\|q) = \sum_{y\in Y}\left\{d(y)\ln\left[\frac{d(y)}{q(y)}\right] - [d(y) - q(y)]\right\}, \quad (14)$$

the terms $g(y:\mu)$ and q are related by the following expression:

$$I\,(d\,\|g(y:\mu)) = \min_{q\in\mu} I\,(d\|q). \quad (15)$$

When $\mu = \hat{\mu}$, the quantity q is equal to g. Hence, the objective of the algorithm is to find the minima of $I(d\|q)$ with respect to $\hat{\mu}(x)$. The terms in the log-likelihood function that depend on the parameter set (attenuation values to be estimated) are negative of the corresponding terms in the I-divergence. Thus, minimizing the I-divergence over the parameter set $\hat{\mu}$ is equivalent to maximizing the log-likelihood function. Minimizing the I-divergence offers the unique advantage that it has a known lower bound (equal to zero), for projection data processed from any system. This is not the case with maximizing the log likelihood as the upper bound is not known. The derivation of the iterative algorithm and its proof is discussed by O'Sullivan and Benac (2007).

Minimizing (14) as per (15) yields (16), the expression for updating the parameter set (attenuation values):

$$\hat{\mu}^{(k+1)}(x) = \hat{\mu}^{(k)}(x) - \frac{1}{Z(x)}\ln\left(\frac{\tilde{b}(x)}{\hat{b}^{(k)}(x)}\right). \quad (16)$$

The terms $\tilde{b}(x)$ and $\hat{b}^{(k)}(x)$ are the back projections of $d(y)$ and the current estimates of $\hat{q}^{(k)}(y)$, respectively. In other words, they are the back projections of the measured data and the nonlinear model employed (based on Beer-Lamberts law). Their expressions are given by

$$\tilde{b}(x) = \sum_{y\in Y} h(y|x)d(y) \quad (17)$$

$$\hat{b}^{(k)}(x) = \sum_{y\in Y} h(y|x)\hat{q}(y) \quad (18)$$

$$\hat{q}^{(k)}(y) = \lambda(y)\exp\left[-\sum_{x\in X} h(y|x)\hat{\mu}^{(k)}(x)\right]. \quad (19)$$

The iterative process for computing the image goes backwards starting from (19) to (16). An initial guess for $\mu^{(k=0)}(x)$ is chosen to calculate $\hat{q}(x)$ in (19); then $\hat{q}(x)$ is used to calculate $\hat{b}(x)$ in (18). The back projection $\tilde{b}(x)$ is computed just once based on $d(y)$. $\mu^{(k+1)}(x)$ is updated based on (16), and the process is started again setting $k = k + 1$ using the updated values of attenuation. A non-negativity constraint is applied on the values of attenuation. Hence at any iteration, if $\hat{\mu}^{(k+1)}(x) < 0$ it is overwritten as $\hat{\mu}^{(k+1)}(x) = 0$. $Z(x)$ in (16) is an appropriate scaling function chosen for the xth pixel such that the following criterion is satisfied (O'Sullivan and Benac 2007):

$$\sum_{x\in X}\left(\frac{h(y|x)}{Z(x)}\right) \leqslant 1. \quad (20)$$

For every pixel x, the length of the longest projection y passing through it was chosen as the value of $Z(x)$ such that (20) was satisfied. The value of $Z(x)$ was found to be insensitive to the final convergence values.

The AM algorithm discussed here does not model Compton scatter. In this study, the gamma ray used (experimental and simulated) includes only the unattenuated gamma ray photons. If the scatter is significant and unavoidable in the scanner, then a more sophisticated algorithm must be used. If the mean scatter is known for a given case, then mathematical strategies have been discussed by O'Sullivan and Benac (2007).

3. Data generation methodology

Transmission data from three different types of phantoms were processed by the algorithms for comparison. The first two cases of the phantom considered were synthetic, as in simulated gamma ray transmission data were generated on the basis of these phantoms and processed. In the third case, experimental transmission data were gathered with a second generation fan beam tomography setup and processed. The holdup distribution images of the liquid and the gaseous phases in the three cases of the phantom are determined and the results are compared.

The first phantom has regions of gas (air) and liquid (water) alone. The second phantom has regions with solid (metal) in addition to gas (air) and liquid (water). The objective of using the second phantom is to test for applications where the solid phase in the system is stationary, as in the case of gamma ray tomography applied to columns with unavoidable internal structures, or those with structured packing or a fixed bed (Roy and Al-Dahhan 2005). In such applications the background scans, or calibration scans, of the column include the solid phase; thereby only the liquid and gaseous phases are accounted for when the dynamic system is imaged. In the third case, experimental data were collected for a phantom with a gaseous phase (air) and a liquid phase (air). Although the gas and liquid phases are stationary in all the phantoms, they are processed assuming them to be dynamic. Hence, the holdup images obtained are meant to provide time-averaged holdup distribution information.

3.1. Details of the phantom

3.1.1. Phantom for simulation (cases I and II). In this study, a synthetic phantom was considered with dimensions as indicated in figure 2.

The diameter of the phantom, D_{col}, was set to 8 in; the other region in the phantom has dimensions that are in proportion to the diameter. The proportionality ratios are indicated in figure 2. In case I, the regions R1 through R4 are filled with air and the background region B is filled with water (table 1).

This represents an ideal two-phase arrangement consisting of liquid and gas. In case II, the regions R1 and R4 are filled with air, the regions R2 and R3 are filled with iron and the background region is filled with water (table 1). The shape of the background region is the same as case I. Case II represents a situation where columns have internal structures that are static

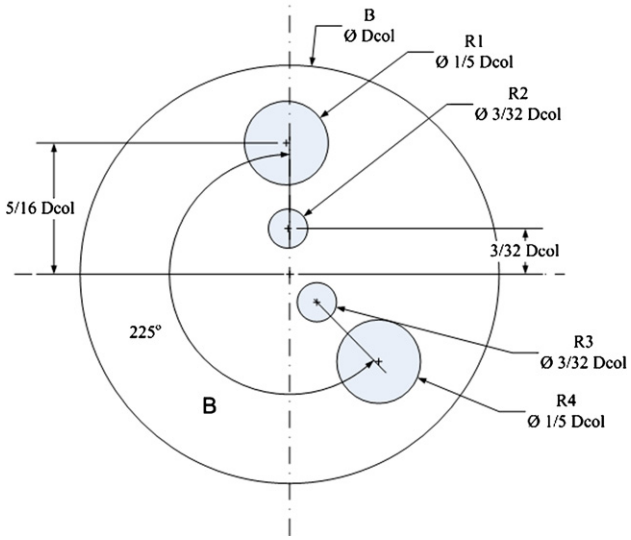

Figure 2. Schematic of phantom for which the data were generated by simulation. $D_{col} = 8$ in. The details of the material in regions R1, R2, R3 and R4 are given in table 1.

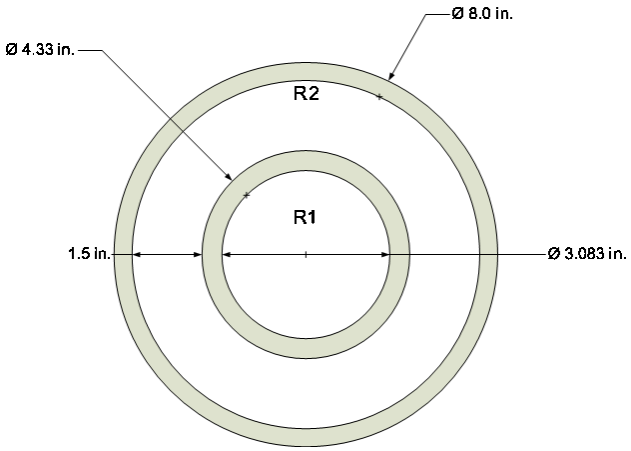

Figure 3. Schematic cross section of the phantom for which experimental transmission data were gathered. The walls are made of Perspex. Region R1 is air and region R2 is filled with water.

and are made of metal which usually have high attenuation values. The holdup images are determined only for the gas and liquid present in the case II phantom.

3.1.2. Phantom for experimental data (case III). A phantom made of Perspex (acrylic glass) with dimensions as indicated in figure 3 is used for case III. This phantom consists of two concentric pipes glued to a flat plate (not shown in the figure). The inner R1 chamber is empty (filled with air) and the outer annular chamber R2 consists of water. This phantom is similar to the phantom in case II (figure 2), as solid material (walls) is present in the domain; however, the attenuation of the Perspex material is far lower than iron or any other metal. Hence, in essence it is a two-phase phantom (like case I) with gas and liquid in a different spatial configuration than case I.

Table 1. Materials used in the phantom and the attenuation values.

Region in phantom (figure 2)	Material used. Attenuation values indicated in parenthesis	
	Case I	Case II
B	Water (0.0863 cm^{-1})	Water (0.0863 cm^{-1})
R1	Air (0.0 cm^{-1})	Air (0.0 cm^{-1})
R2	Air (0.0 cm^{-1})	Iron (0.2197 cm^{-1})
R3	Air (0.0 cm^{-1})	Iron (0.2197 cm^{-1})
R4	Air (0.0 cm^{-1})	Air (0.0 cm^{-1})

3.2. Details of the gamma ray computer tomography (CT) scanner

Figure 4 shows the schematic of the CT scanner used in this study for gathering the experimental data for the case III phantom. The dimension of this same scanner was used to generate the simulated data for the phantom (cases I and II) in figure 2. The scanner consists of a point ^{137}Cs gamma ray source that has a photo peak at 660 keV. The attenuation data shown in table 1 are based on this energy of the gamma ray photons. An equiangular fan beam arrangement of the source and the detectors is used. The source is at the pointed end of the fan and the detectors are at the curved end of the fan, placed 120 cm apart. The detector arrangement consists of nine 2 in diameter NaI(Tl) detectors of 2 in thickness. Each of these detectors is collimated with a lead collimator that is about 2.5 in thick and has an open aperture of dimension 1/16 in $\times$ 3/16 in. This aperture reduces the effective exposed area of the crystal to a rectangular region of dimension 1/16 in $\times$ 3/16 in. The counts received by the detectors are limited to what is incident on this aperture. This detector array is moved with a motor 21 times at an angle of 0.13° from the source, thereby creating 189 detector positions effectively for each source position. The projection is modeled as a fine line between the source and the detector as the open area of the detectors is very small. A total of 197 source positions (also called views) are considered; hence, gamma ray count data for 189 $\times$ 197 (total 37 233) projections passing through the domain are collected. The gamma ray count data recorded are energy thresholded; hence unattenuated gamma ray photon counts of 660 keV were recorded. The simulated data for the phantom are generated for 189 projections per view for 197 views, based on the same geometry as the scanner described above. An 80 $\times$ 80 pixels resolution is used to reconstruct the image. Hence, each pixel represents an area of 2.54 mm $\times$ 2.54 mm of the phantom. Details of the data acquisition hardware, collimators and detectors used to collect the photon count data are available from Roy (2006).

3.3. Gamma ray count data generation

Gamma ray count data were generated by simulation for cases I and II of the phantom. Schaffer's (1970) algorithm is used to generate the counts I that are Poisson random numbers with probability P_I and mean $g(y : \mu_{\text{phantom}})$ given by

$$P_I = \frac{[g(y : \mu_{\text{phantom}})]^I}{I!} \exp[g(y : \mu_{\text{phantom}})] \qquad (21)$$

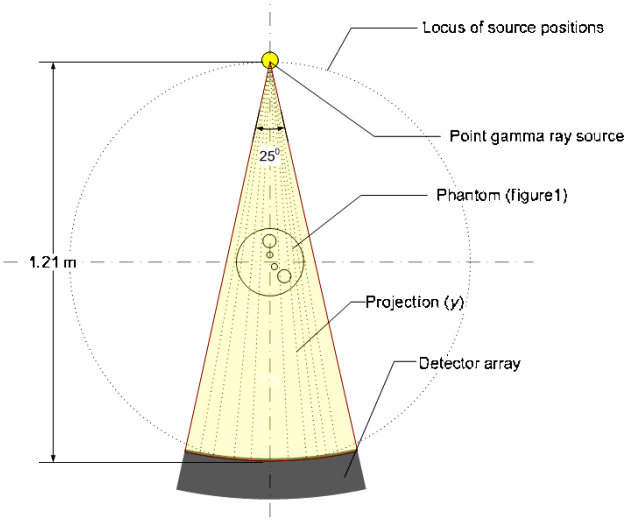

Figure 4. Schematic of the scanner arrangement with the phantom in the center. A gamma ray fan beam with a 25° angle and a detector array with nine detectors are used (not shown). These detectors are moved through 21 positions effectively creating 189 projections. The region occupied by the detectors is indicated as the detector array. The source, and the detector array, is moved along the locus as indicated for 197 positions and projection data for each location are gathered.

$$g(y : \mu_{\text{phantom}}) = \lambda(y) \exp\left[-\sum_{x \in X} h(x|\, y)\mu_{\text{phantom}}(x)\right]. \quad (22)$$

This Poisson number generated for each y is set equal to $d(y)$, the counts received by the detector. The attenuation value $\mu_{\text{Phantom}}(x)$ used to generate the count data is the attenuation of the xth pixel in the phantom (figure 1) along projection y. The algorithms (AM and EM) determine these values without any prior information about the phantom and based purely on the Poisson numbers.

To reduce the effect of noise and uncertainty in the data and to get a better quality of the images, the mean value of the counts based on multiple samples or readings for a given projection y is often used for processing the data, as represented by (23). Here, n represents the number of data samples of counts for a given projection y,

$$d(y) = \frac{1}{n}\sum_{i=1}^{n} I_i. \quad (23)$$

If an infinite number of samples are collected, then (24) would give an accurate value of the mean $g(y : \mu_{\text{phantom}})$:

$$\lim_{n \to \infty} \frac{1}{n}\sum_{i=1}^{n} I_i = g(y : \mu_{\text{phantom}}). \quad (24)$$

Hence, when (23) is used with some small finite values of n then it can be said that an approximate estimate of the mean $g(y : \mu_{\text{phantom}})$ is used to process the data. To see how the number of data samples used to arrive at the mean value of the counts affects the AM and EM algorithms' performance, the mean of multiple samples (n) of I (ranging from 1 to 100) is used as estimates of $g(y : \mu_{\text{phantom}})$ for $d(y)$ as per (23). It can be seen as follows: the higher the number of samples, the less noise in the data. This procedure was also followed with the experimental data collected with the scanner for the case III phantom. The maximum value of $n = 100$ is an optimum choice as the results discussed in section 4 show that the maximum difference in the reduction of noise, and by extension error, in the holdup images occurs for lower values of n. Hence, the reduction in error from $n = 1$ to $n = 5$ is far greater than the reduction in error from $n = 50$ to $n = 100$. The value for $n = 100$ is also practical when data are collected with the scanner, as higher values would dramatically increase the time required to execute the scan without an increase in accuracy commensurate with it.

4. Calculation of holdup distribution

The count data generated by simulation are processed by the algorithms (AM and EM) which reconstruct an image that depicts the attenuation image, $\hat{\mu}_{l-g}(x)$, of the scanned domain. This attenuation value is a linear sum of the product of the holdup fractions of the phases and their pure attenuation values as given by (25)

$$\hat{\mu}_{l-g}(x) = \hat{\mu}_l(x)\varepsilon_l(x) + \hat{\mu}_g(x)\varepsilon_g(x). \quad (25)$$

The subscripts l and g represent liquid and gas, respectively, $\varepsilon(x)$ represents the holdup fraction and $\hat{\mu}(x)$ represents the attenuation of the pure phase. The objective of using CT is to determine the values of $\varepsilon(x)$. The $\hat{\mu}(x)$ values for liquid and gas are usually determined by a background scan where the domain purely consists of only one of the phases. In addition, it is also known that the sum of the holdup fractions of the two phases is unity

$$\varepsilon_l(x) + \varepsilon_g(x) = 1. \quad (26)$$

To determine the gas holdup for the case I phantom, equations (25) and (26) are combined with the assumption that $\hat{\mu}_g(x)$ (representing the calibration attenuation image of the system filled with gas) should be equal to zero, to give (27). This assumption is reasonable as air has a negligible contribution to the attenuation of a gamma ray photon with 661 keV energy. Hence, the gas holdup distribution image is determined using (27), and by extension the liquid holdup distribution image by using (28):

$$\varepsilon_g(x) = \frac{\hat{\mu}_l(x) - \hat{\mu}_{l-g}(x)}{\hat{\mu}_l(x)} \quad (27)$$

$$\varepsilon_l(x) = 1 - \frac{\hat{\mu}_l(x) - \hat{\mu}_{l-g}(x)}{\hat{\mu}_l(x)} \quad (28)$$

In (27) and (28), $\hat{\mu}(x)_{l-g}$ represents the attenuation image of the phantom with the region B filled with water and regions R1 through R4 filled with air, and $\hat{\mu}(x)_l$ represents the attenuation image of the phantom with regions B and R1 through R4 filled with water.

For the cases II and III of the phantom which has solid internals, attenuation images $\hat{\mu}(x)_{l-g}$ and $\mu(x)_l$ in (25) are replaced with $\hat{\mu}(x)_{l-g-s}$ and $\hat{\mu}(x)_{l-s}$, respectively, to give

$$\varepsilon_g(x) = \frac{\hat{\mu}_{l-s}(x) - \hat{\mu}_{l-g-s}(x)}{\hat{\mu}_{l-s}(x)}. \quad (29)$$

The image $\hat{\mu}(x)_{l-g-s}$ has liquid in region B, gas in regions R1 and R4, and solid in regions R2 and R3 of the phantom (figure 2), and region R1 with gas and region R2 with liquid in the case III phantom. The background scan image $\hat{\mu}(x)_{l-s}$ has liquid in regions B, R1 and R4, and solid in regions R2 and R3 of the case II phantom (figure 2) and liquid in R1 and R2 of the case III phantom (figure 3).

Similarly, to determine the liquid holdup image for the case II of the phantom, (28) is modified substituting $\hat{\mu}(x)_l$ with $[\hat{\mu}_{L-S}(x) - \hat{\mu}_{G-S}(x)]$ to give (30). The image $\hat{\mu}(x)_{g-s}$ has gas in regions B, R1 and R4, and solid in regions R2 and R3 of the case II phantom (figure 2) and gas in R1 and R2 of the case III phantom (figure 3)

$$\varepsilon_l(x) = 1 - \frac{[\hat{\mu}_{L-S}(x) - \hat{\mu}_{G-S}(x)] - \hat{\mu}_{l-g}(x)}{[\hat{\mu}_{L-S}(x) - \hat{\mu}_{G-S}(x)]}. \qquad (30)$$

The attenuation image $\mu(x)$ for different configurations as indicated above is calculated using the AM and EM algorithms. The holdup distribution images are determined post-attenuation image reconstruction based on (27) through (30), for the liquid and the gaseous phases for all three phantom cases. Although the algorithm reconstructs the attenuation images, the holdup distribution images obtained on its basis are analyzed to evaluate the AM and EM algorithms. This is done as ultimately the phase holdup images are of interest to obtain quantitative information about the system being scanned.

5. Results and discussion

The holdup images reconstructed based on simulated transmission data for case I and case II phantoms and experimental transmission data from the case III phantom are analyzed in this section. The mean percentage error and the standard deviation of all the pixels in a given domain with a phantom are used as parameters to qualitatively assess the images. The error values used in this discussion are calculated by comparing the ideal values of holdup with the values of holdup from the reconstructed images.

5.1. Gas holdup images

Using (27) and (29), the gas holdup images were successfully obtained. Figures 5–7 show the gas holdup images obtained using AM, EM and FBP algorithms respectively.

Clearly, both the AM and EM algorithms are able to successfully image the gas phase distribution in all three phantoms as the gas-filled regions are captured in the image with holdup values close to unity. There is no distortion in the reconstructed images; the geometric shapes of the domains (R1 through R4) for case I, R1 and R2 for case II and R1 for case III are maintained and appear just as in the phantom. The transition in the gas holdup values at the edge of the domain is sharper in images generated by the AM algorithm (figure 5) as compared to those by the EM algorithm (figure 6). The AM algorithm provides gas holdup images with uniformity in the domains of the phantom (for all cases of the phantom) where gas is present. These images also confirm that (29) is correctly formulated as complicated arrangements that have parts of the domain covered by the solid material (figures 6(*b*) and (*c*)) in the phantoms are not misrepresented as part of the gas holdup.

In contrast, the FBP results (figure 7) show artifacts especially in the case III phantom. The circular domains R1 and R4 in case I and case II create a shadow in the image. The case III phantom has circular artifacts present. Clearly, the AM and EM gas holdup images have less error than the FBP image.

5.2. Quantitative analysis of gas holdup

A quantitative analysis of the images is possible only when the holdup values of all pixels in a given part of the image are analyzed for error and standard deviation. Standard deviation indicates the level of noise in the image. If the standard deviation of the pixels is high, it means that the image is noisy and a lot of freckles or grains can be seen. The most desirable situation is the one where both the standard deviation and the error are nil. When the standard deviation is small and the error is high, then there is a bias in the image.

Figure 8 shows the mean percentage error and figure 9 shows the standard deviation in the gas holdup values for the three cases of the phantom obtained using both the AM and the EM algorithms. Clearly, the error values in figure 8 show that the AM algorithm performs better than the EM algorithm for any condition of the number of data samples or iterations covered in all the phantoms. When transmission data with low levels of noise ($n = 100$ in (22)) are used, the EM algorithm still gives higher error than the AM algorithm; this is more prominent in the case III phantom. For the case II phantom (figure 8(*b*)), the difference in error between the two algorithms is almost an order of magnitude. This indicates that in the presence of high attenuation material, the AM algorithm gives a more accurate estimate of gas holdup.

The standard deviation of the pixels from the regions of a phantom where gas is present has trends similar to the error values for any given number of iterations and number of transmission data samples for the projections (based on (23)). The values are lower for the results obtained from the AM algorithm as compared to the EM algorithm. As the iterations progress, the standard deviation values stabilize. This indicates that the gas holdup images have less noise in the image. At this point, it is important to determine the standard deviation of the gas holdup in the pixels from the region of the phantom that does not have gas. Ideally, the holdup values and standard deviation in this region should be zero. However, small values are observed.

Figure 10 shows the standard deviation values of the gas holdup in these regions. Again, for all the cases the AM algorithm gives values that are smaller than the EM; hence the noise in the image in these regions is much less.

5.3. Liquid holdup

The liquid holdup images were successfully obtained by using (28) for the case I phantom and (30) for cases II and III.

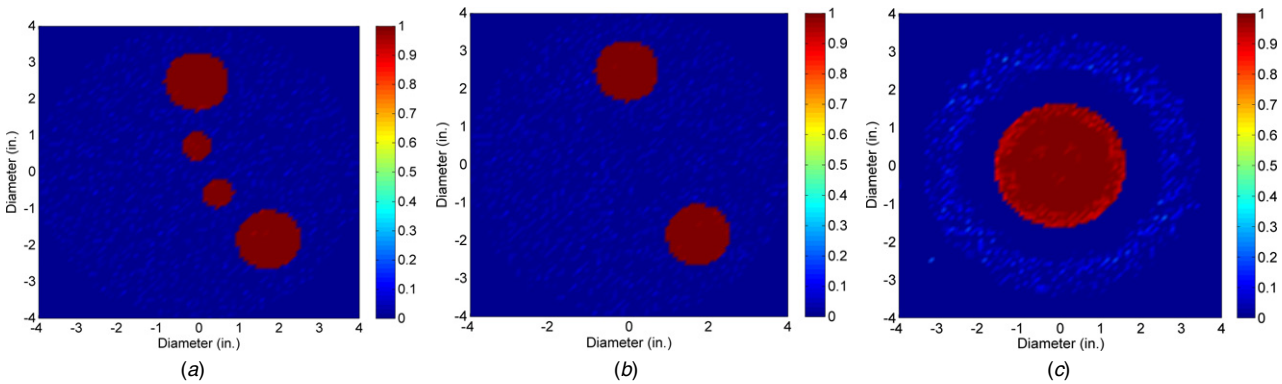

Figure 5. Gas holdup images obtained with the AM algorithm (after 1000 iterations with $n = 50$). The color bar represents the color code used for representing gas holdup values in the images: (*a*) gas holdup based on (27) for the case I phantom (figure 2), (*b*) gas holdup based on (29) for the case II phantom (figure 2) and (*c*) gas holdup based on (29) for the case III phantom (figure 3).

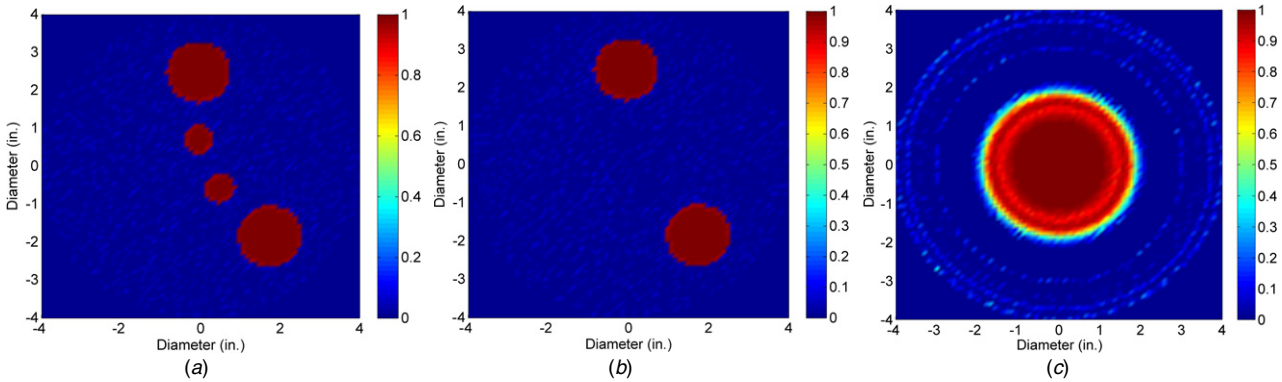

Figure 6. Gas holdup images obtained with the EM algorithm (after 1000 iterations with $n = 50$). The color bar represents the color code used for representing liquid holdup values in the images. (*a*) Gas holdup based on (27) for the case I phantom (figure 2), (*b*) gas holdup based on (28) for the case II phantom (figure 2) and (*c*) gas holdup based on (29) for the case III phantom (figure 3).

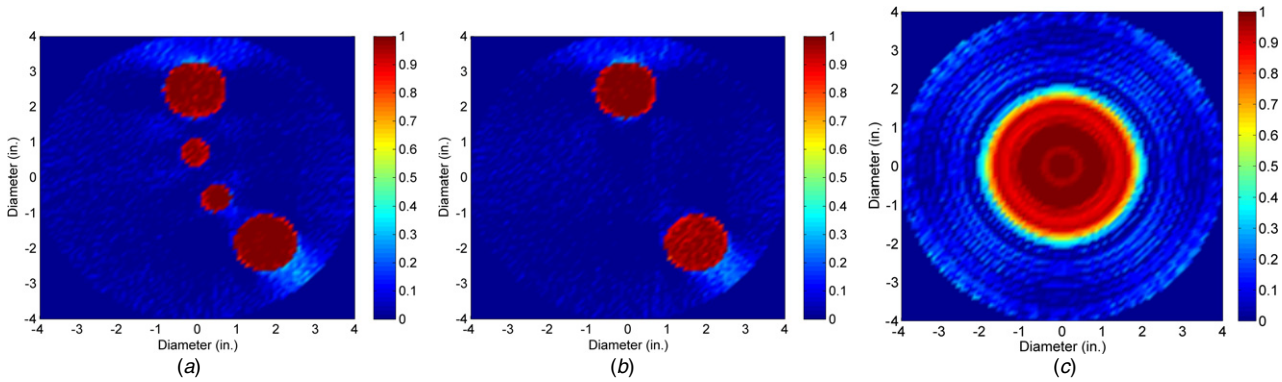

Figure 7. Gas holdup images obtained using the FBP (with $n = 50$). The color bar represents the color code used for representing liquid holdup values in the images. (*a*) Gas holdup based on (27) for the case I phantom (figure 2), (*b*) gas holdup based on (28) for the case II phantom (figure 2) and (*c*) gas holdup based on (29) for the case III phantom (figure 3).

Figures 11–13 show the liquid holdup images obtained using AM, EM and FBP algorithms respectively. Clearly, the liquid phase is separated successfully in these images. The results from the AM and EM algorithms show that there is no distortion in the images; the shapes of the region with liquid in the phantoms are successfully captured. The regions of the case II and III phantoms that have solids are not misrepresented as liquid holdup in the images. As in the case of the gas holdup images, the liquid holdup images have sharper transitions at the edge of the domain when the AM algorithm is used. The effectiveness of the AM algorithm in this aspect can clearly be seen in the case III phantom where actual experimental transmission data are used, by comparing figures 11(*c*) and 12(*c*).

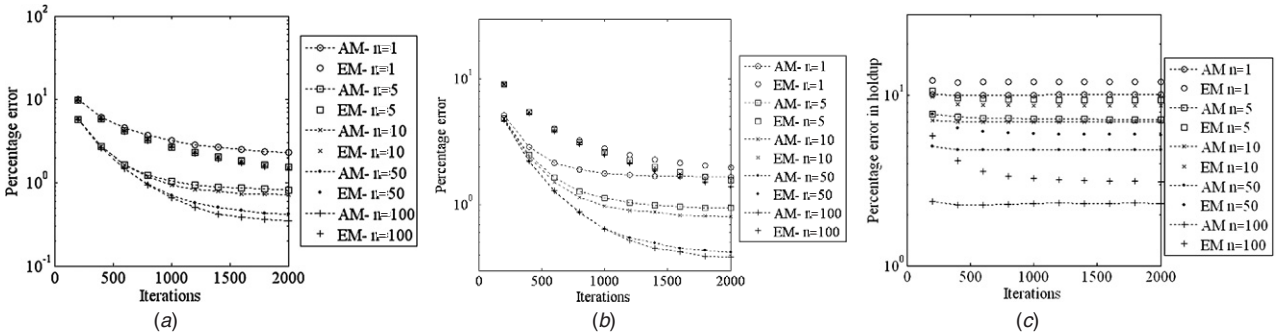

Figure 8. Mean percentage error in gas holdup for results obtained with AM and EM algorithms for projection data with $n = 1$ through $n = 100$ (in (23)). (*a*) Error in gas holdup value for pixels of regions R1, R2, R3 and R4 (figure 2) of the case I phantom; (*b*) error in gas holdup value for pixels in regions R1 and R2 for the case II phantom (figure 2) and (*c*) error in gas holdup value for pixels from the region R1 of the case III phantom (figure 3).

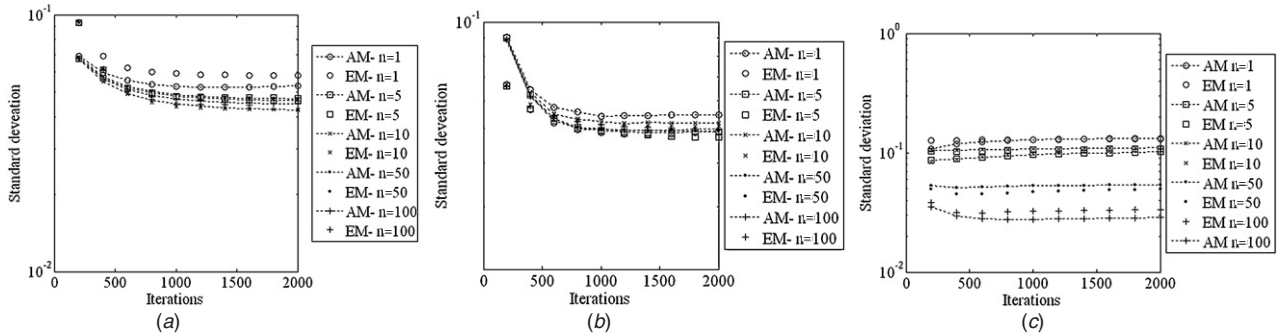

Figure 9. Standard deviation of gas holdup for results obtained with AM and EM algorithms for projection data with $n = 1$ through $n = 100$ (from (23)). (*a*) Standard deviation of gas holdup in pixels of regions R1, R2, R3 and R4 (figure 2) of the case I phantom; (*b*) standard deviation of gas holdup in pixels of regions R1 and R2 for the case II phantom (figure 2) and (*c*) standard deviation of gas holdup in pixels of region R1 of the case III phantom (figure 3).

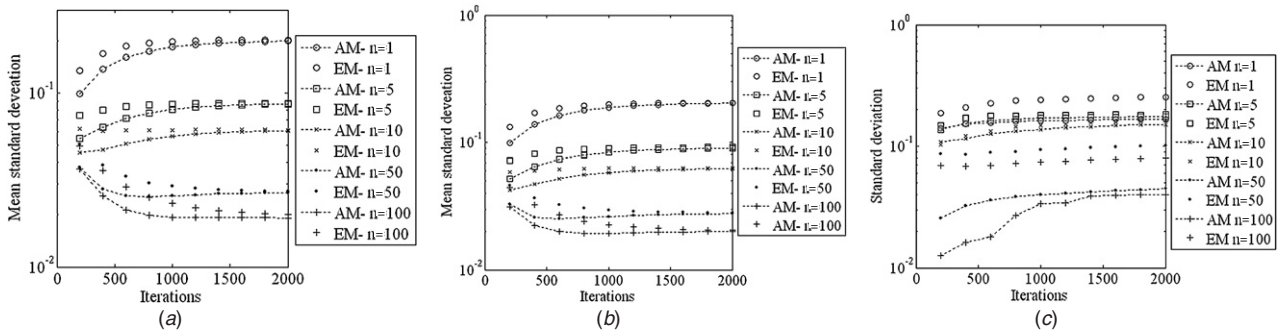

Figure 10. Standard deviation values of gas holdup from the results obtained in regions of the phantoms where ideally the gas holdup is zero. The values obtained with AM and EM algorithms for projection data with $n = 1$ through $n = 100$ are shown. (*a*) Standard deviation of gas holdup in pixels of region B (figure 2) of the case I phantom, (*b*) standard deviation of gas holdup in pixels of regions B, R3 and R4 for the case II phantom (figure 2) and (*c*) standard deviation of gas holdup in pixels of region R2 of the case III phantom (figure 3).

In cases I and II the phantom is pixilated such that only one phase is present in any pixel. In the case III phantom, it is not possible to control this and the pixel along the curved boundary of the R2 domain (figure 3) tends to smudge. In spite of this, the AM algorithm gives better results than the EM algorithm as the edges of the liquid region appear to be blurred. For the case II phantom, the liquid holdup image obtained with the EM algorithm (figure 12(*b*)) has freckles, and hence has more noise, compared to the one obtained with the AM algorithm (figure 11(*b*)). Also the holdup in the region occupied by the high attenuation material (R3 and R4 in figure 3) in the EM algorithm image is slightly above zero. Both these aspects are attributed to the presence of the high attenuation material present in the domain.

The FBP holdup images show artifacts similar to the gas holdup images. There is a shadow created by the circular gas holdup regions of the domain. For the case II phantom, the metallic regions R2 and R3 created the most pronounced artifacts. The circular shape of domains R3 and R4 is lost, and most of this region appears as part of the liquid holdup

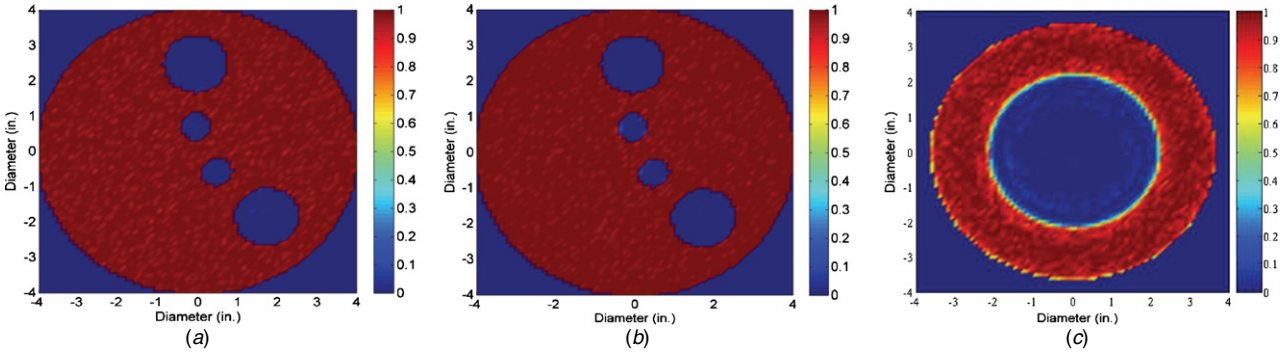

Figure 11. Liquid holdup images obtained with the AM algorithm (after 1000 iterations with $n = 50$). The color bar represents the color code used for representing liquid holdup values in the images: (*a*) liquid holdup based on (28) for the case I phantom (figure 2), (*b*) liquid holdup based on (30) for the case II phantom (figure 2) and (*c*) liquid holdup based on (30) for the case III phantom (figure 3).

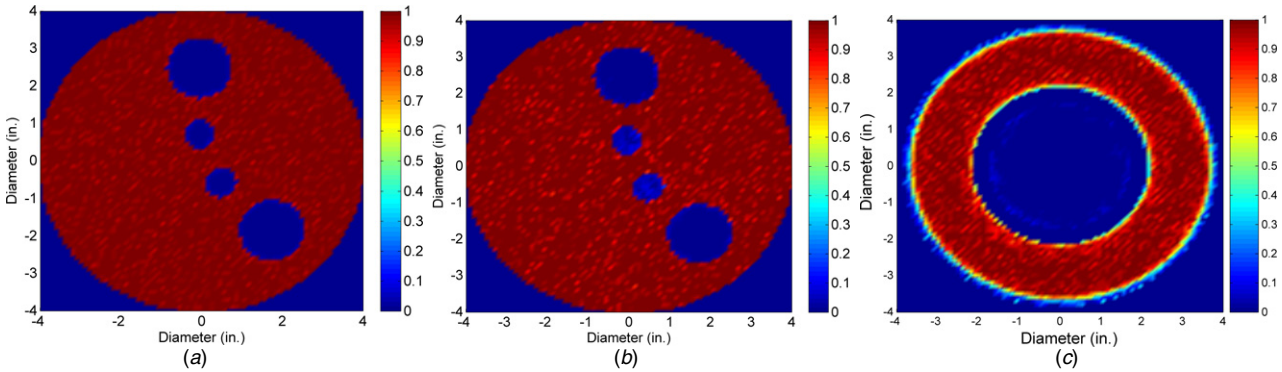

Figure 12. Liquid holdup images obtained with the EM algorithm (after 1000 iterations with $n = 50$). The color bar represents the color code used for representing liquid holdup values in the images: (*a*) liquid holdup based on (28) for the case I phantom (figure 2), (*b*) liquid holdup based on (30) for the case II phantom and (*c*) liquid holdup based on (30) for the case III phantom.

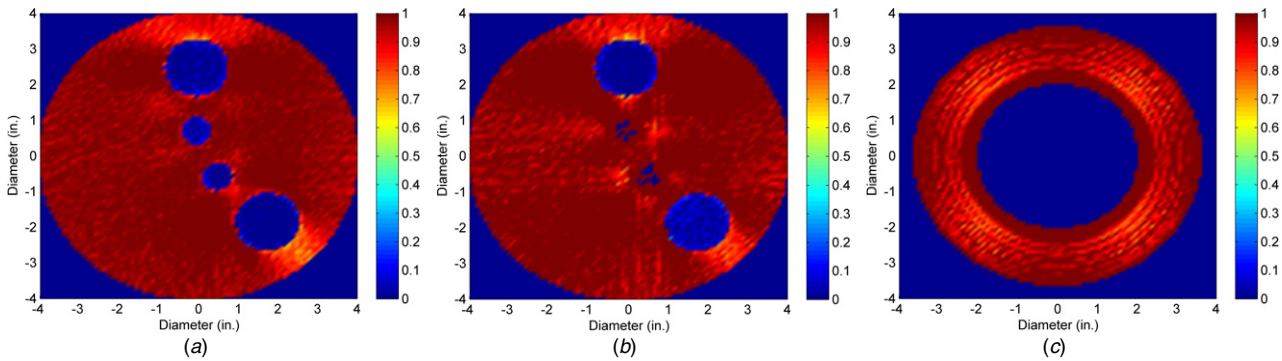

Figure 13. Liquid holdup images obtained using the FBP method (with $n = 50$). The color bar represents the color code used for representing liquid holdup values in the images: (*a*) liquid holdup based on (28) for the case I phantom (figure 2), (*b*) liquid holdup based on (30) for the case II phantom and (*c*) liquid holdup based on (30) for the case III phantom.

distribution (figure 13(*b*)). The high attenuation domain severely affects the FBP results.

5.4. Quantitative analysis of liquid holdup

Figure 14 shows the mean percentage error in estimating the liquid holdup values in the region of the phantoms filled with the liquid. Clearly, for all three phantom cases the AM algorithm performs better universally than the EM algorithm. For the case II phantom, there is an order of magnitude difference in the error between the holdup value results from both the algorithms.

Also, the error does not stabilize or reduce for data with higher noise levels (lower values of n as per (23)) when the EM algorithm is used for this phantom case. It should be noted that the liquid domains in the phantoms of cases I and II are physically similar. This clearly shows that the holdup image of a phase that does not have a high attenuation is affected by parts of the domain that have high attenuating material or phase.

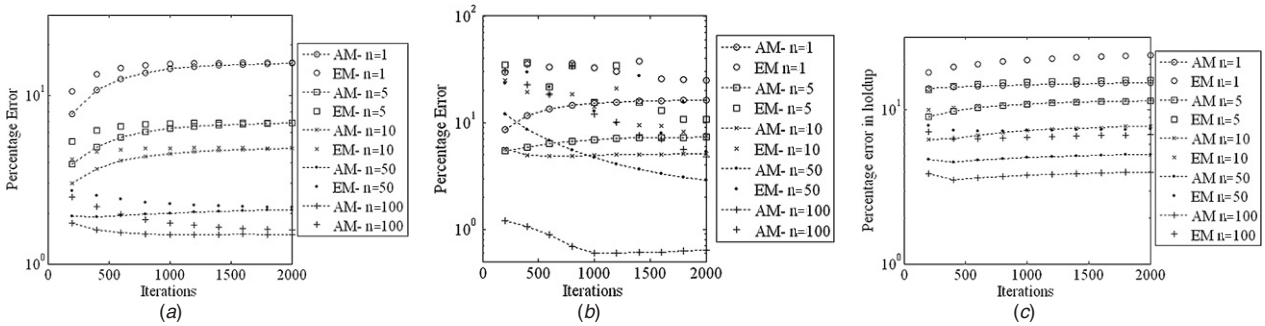

Figure 14. Mean percentage error in liquid holdup for results obtained with AM and EM algorithms for projection data with $n = 1$ through $n = 100$. (*a*) Error in liquid holdup for pixels of region B (figure 2) of the case I phantom, (*b*) error in liquid holdup value for region B for the case II phantom (figure 2) and (*c*) error in the liquid holdup value in region R2 of the case III phantom (figure 3).

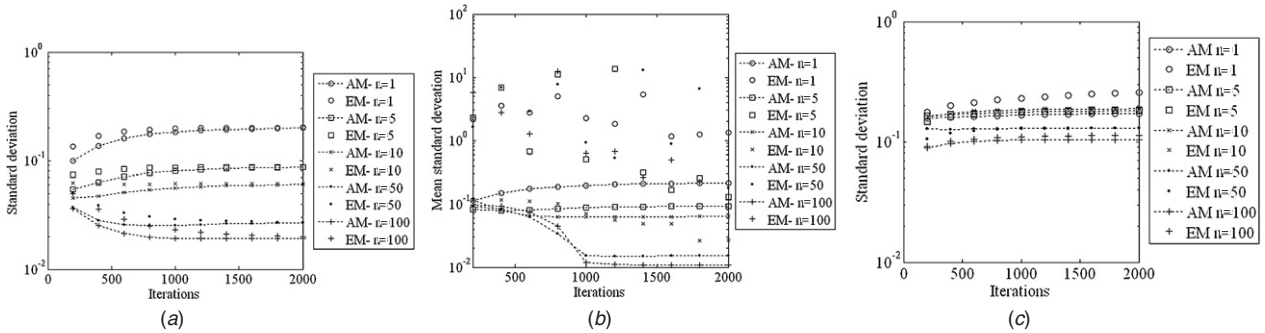

Figure 15. Standard deviation in liquid holdup for results obtained with AM and EM algorithms for projection data with $n = 1$ through $n = 100$. (*a*) Standard deviation in liquid holdup of pixels of region B (figure 2) of the case I phantom, (*b*) standard deviation in liquid holdup of region B for the case II phantom (figure 2) and (*c*) standard deviation in liquid holdup of region R2 of the case III phantom (figure 3).

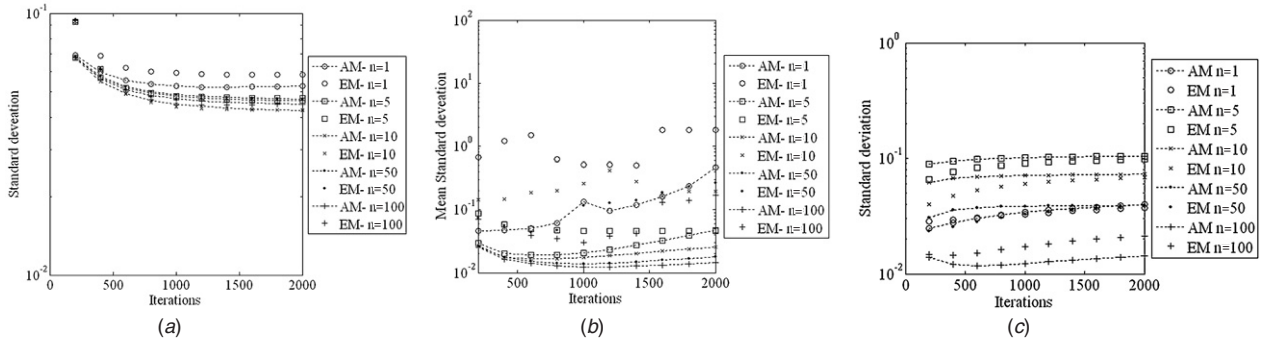

Figure 16. Standard deviation values of liquid holdup results obtained in regions of the phantoms where liquid holdup is ideally zero. The values obtained with AM and EM algorithms for projection data with $n = 1$ through $n = 100$ are shown. (*a*) Standard deviation of liquid holdup in pixels of regions R1, R2, R3 and R4 (figure 2) of the case I phantom; (*b*) standard deviation of liquid holdup in pixels of region R1, R2, R3 and R4 for the case II phantom (figure 2) and (*c*) standard deviation of gas holdup in pixels of the region R1 of the case III phantom (figure 3).

The AM algorithm provides images with better quality in such applications as compared to the EM algorithm.

Figure 15 shows the standard deviation of the liquid holdup from the pixels that are from the region of the phantom that have the liquid phase.

The results from the AM algorithm have a lower standard deviation compared to the EM algorithm for any value of the iterations or the number of data samples per projection (as per (23)). This trend is true for all the phantoms studied. This indicates that the noise levels in the images obtained using the AM algorithm are much lower than what is seen in results from the EM algorithm. For the case II phantom, the standard deviation values of the results from the EM algorithm are an order of magnitude different compared to the AM, reconfirming what was seen for the same case in figure 14.

The standard deviation and percentage error for transmission data with lower n values are found to increase with the increase in the number of iterations for both the liquid and gas holdup images. This phenomenon is known to occur with EM (Snyder *et al* 1987) and AM (Benac 2005) algorithms due to the random nature of the data. This happens even as the solution converges toward a maximum log-likelihood estimate.

Snyder *et al* (1987) have suggested strategies that overcome this problem which have not been implemented here as it is out of the scope of this study. The images reconstructed using the AM algorithm exhibit this behavior to a far less extent at lower iterations compared to the EM algorithm.

Figure 16 shows the standard deviation values of liquid holdups from pixels from the regions of the phantoms that do not have the liquid in them. Ideally, these values should be zero and by extension the standard deviation of this should be zero. However, some small finite values of holdup are obtained. Here again the results from the AM algorithm show values of standard derivations that are much lower than the EM algorithm for all cases, as the noise level in the images is lower with the use of the AM algorithm. The reduction in values of standard deviation by the AM algorithm is more prominent in the case II phantom where a high attenuation material (solid) is present in the domain.

6. Conclusions

The AM algorithm was successfully implemented for the case of single energy gamma ray tomography to determine phase holdup images for two phase systems for phantoms with different configurations. The performance of the algorithm was compared by putting the effect of some critical parameters, such as the noise level in the data and the number of iterations used to reconstruct the image, in perspective. A systematic quantitative analysis of the holdup distribution images generated using the AM and EM algorithms was carried out for three phantom cases. The AM and EM images were compared to the FBP images. The AM algorithm proposed by O'Sullivan and Benac (2007) performs better than the EM algorithm proposed by Lange and Carson (1984) when used for gamma ray tomography to determine holdup images in two phase systems. The holdup images obtained with the FBP are less accurate than the AM and EM results. The results show an overall improvement in the quality of the image in terms of the noise and accuracy of the estimated values when the AM algorithm is used. For data with high noise the AM algorithm gives less error when compared to EM and FBP algorithms, and it requires fewer iterations to reach a given level of accuracy. For applications that involve the use of highly attenuating material the AM algorithm is more stable and produces holdup images that have a greater degree of accuracy and lower levels of noise. This is true for both parts of the domain that have the high attenuation material (metals) and parts that do not have it, like the surrounding areas (liquid and gas).

The differences in the performance of the two stochastic algorithms could be attributed to the simplification introduced in the M-step of the EM algorithm as indicated in (8) to estimate (7). In spite of using three terms of (8) (shown in (9)) for the EM algorithm, as recommended by Lange and Carson (1984) for maximum accuracy in the results, it does not match the performance of the AM algorithm; the AM algorithm performs better. Hence, the AM algorithm is a better choice for image reconstruction for determining the holdup distribution images in multiphase systems involving two-phase flow.

Acknowledgments

The authors would like to acknowledge the United States Department of Energy for sponsoring the research project (identification number: DE-FC-36-01GO11054) and David G Politte for helping with the implementation of the filter back projection algorithm.

References

Benac J 2005 Alternating minimization algorithms for x-ray computed tomography: multigrid acceleration and dual energy application *DSc* Washington University, St Louis, MO

Bieberle M and Hampel U 2006 Evaluation of a limited angle scanned electron beam x-ray CT approach for two-phase pipe flows *Meas. Sci. Technol.* **17** 2057–65

Browne J A and Holmes T J 1992 Developments with maximum likelihood x-ray computed tomography *IEEE Trans. Med. Imaging* **11** 40–52

Csiszár I 1991 Why least squares and maximum entropy? An axiomatic approach to inference for linear inverse problems *Ann. Stat.* **19** 2033–66

Kak A C and Slaney M 1988 *Principles of Computerized Tomographic Imaging* vol 3 (New York: IEEE) pp 83–6

Khopkar A R, Rammohan A R, Ranade V V and Dudukovic M P 2005 Gas–liquid flow generated by a Rushton turbine in stirred vessel: CARPT/CT measurements and CFD simulations *Chem. Eng. Sci.* **60** 2215–29

Kumar S and Duduković M P 1997 Computer assisted gamma and x-ray tomography: applications to multiphase flow systems *Non-Inavsive Monitoring of Multiphase Flows* eds J Chaouki, F Larachi and M P Duduković (Amsterdam: Elsevier) chapter 2

Kumar S B, Moslemian D and Dudukovic M P 1997 Gas-holdup measurements in bubble columns using computed tomography *AIChE J.* **43** 1414–25

Lange K and Carson R 1984 EM reconstruction algorithims for emission and transmission tomography *J. Comput. Assist. Tomogr.* **8** 306–16

Ollinger J M 1994 Maximum-likelihood reconstruction of transmission images in emission computed tomography via the EM algorithm *IEEE Trans. Med. Imaging* **13** 89–101

O'Sullivan J A and Benac J 2007 Alternating minimization algorithms for transmission tomography *IEEE Trans. Med. Imaging* **26** 283–97

Roy S 2006 Phase distribution and performance studies of gas-liquid monolith reactor *DSc* Washington University, St Louis, MO

Roy S and Al-Dahhan M 2005 Flow distribution characteristics of a gas–liquid monolith reactor *Catal. Today* **105** 396–400

Roy S, Chen J, Kumar S B, Al-Dahhan M H and Dudukovic M P 1997 Tomographic and particle tracking studies in a liquid–solid riser *Ind. Eng. Chem. Res.* **36** 4666–9

Roy S, Kemoun A, Al-Dahhan M H, Dudukovic M P, Skourlis T B and Dautzenberg F M 2004 Countercurrent flow distribution in structured packing via computed tomography *Chem. Eng. Process.* **44** 59–69

Schaffer H E 1970 Algorithms 369: generation of random numbers satisfying the Poisson distribution *Commun. ACM* **13** 49–51

Snyder D L and Cox J J R 1977 An overview of reconstructive tomography and limitations imposed by a finite number of projections *Reconstruction Tomography in Diagnostic Radiology and Nuclear Medicine* ed M M Ter-Pogossian (Baltimore, MD: University Park Press)

Snyder D L, Schulz T J and O'Sullivan J A 1992 Deblurring subject to nonnegativity constraints *IEEE Trans. Signal Process.* **40** 1143–50